Catalysis Today xxx (xxxx) xxx–xxx

Contents lists available at ScienceDirect

Catalysis Today

journal homepage: www.elsevier.com/locate/cattod

CO and CO_2 methanation over Ni/Al@Al_2O_3 core–shell catalyst

Thien An Le, Jieun Kim, Jong Kyu Kang, Eun Duck Park*

Department of Chemical Engineering and Department of Energy Systems Research, Ajou University, 206, World cup-ro, Yeongtong-Gu, Suwon 16499, Republic of Korea

ARTICLE INFO

Keywords:
Ni catalyst
γ-Al_2O_3
Al@Al_2O_3
CO methanation
CO_2 methanation
deposition–precipitation method

ABSTRACT

Core–shell Al@Al_2O_3, which was obtained by hydrothermal surface oxidation of Al metal particles, was used as the support in supported Ni catalysts for CO and CO_2 methanation. The core–shell micro-structured support (Al@Al_2O_3) helped develop a highly efficient Ni-based catalyst compared with conventional γ-Al_2O_3 for these reactions. Moreover, the deposition–precipitation method was shown to outperform the wet impregnation method in the preparation of the active supported Ni catalysts. The catalysts were characterized using various techniques, namely, N_2 physisorption, H_2 chemisorption, CO_2 chemisorption, temperature-programmed reduction with H_2, temperature-programmed desorption after CO_2 adsorption, X-ray diffraction, inductively coupled plasma-atomic emission spectroscopy, high-resolution transmission electron microscopy, and in situ diffuse reflectance infrared Fourier transform spectroscopy. Higher Ni dispersion when using Al@Al_2O_3 as the support and the deposition–precipitation method resulted in better catalytic performance for CO methanation. Furthermore, the higher density of medium basic sites and enhanced CO_2 adsorption capacity observed for Ni/Al@Al_2O_3 helped increase catalytic activity for CO_2 methanation.

1. Introduction

CO_2 conversion technologies are crucial for mankind, given their ability to mitigate global warming [1]. Since CO_2 is the most stable and fully oxidized state of carbon, its chemical transformation requires other highly reactive chemicals [2] or additional energy [3,4]. In order to convert CO_2 into energy or chemical feedstock without net production of CO_2 in the overall process, renewable energy should be used directly [5] or indirectly [6]. The electrolysis of water using electricity from wind or solar energy is an example of the indirect utilization of renewable energy to produce H_2. Power-to-gas (P2G) is the concept that surplus electricity from a renewable energy source can be stored or distributed in the form of synthetic natural gas which can be produced from H_2 and carbon oxides (CO and CO_2) [7]. The carbon oxides can be supplied by a carbon capture and storage facility or synthesized on site by gasification of biomass or organic wastes [8].

The Sabatier reaction involves the synthesis of CH_4 from H_2 and carbon oxides (CO and CO_2) as follows.

$$CO\ (g) + 3H_2\ (g) \leftrightarrow CH_4\ (g) + H_2O\ (g)\ \Delta H^o_{298\,K} = -206\,kJ/mol \quad (1)$$

$$CO_2\ (g) + 4H_2\ (g) \leftrightarrow CH_4\ (g) + 2H_2O\ (g)\ \Delta H^o_{298\,K} = -165\,kJ/mol \quad (2)$$

Since these reactions are thermodynamically limited and highly exothermic, the low-temperature operation is preferred to achieve high single-pass conversion. Moreover, temperature control while designing the catalyst and reactor is essential to prevent the formation of hotspots. From this viewpoint, the development of a very active catalyst at low temperatures as well as the application of highly thermal conduction material is extremely desirable.

Until now, Ni-based catalysts have been widely used in the industrial process because of their relative fair activity, low cost, and high availability [9–17]. Various supports such as Al_2O_3 [10,11,18], CeO_2 [10,19–21], ZrO_2 [10,22], CeO_2-ZrO_2 [9,20], SiO_2 [10,14,18,23,24], Y_2O_3 [22,25], or zeolites [18,23,26] combined with novel preparation methods [9,12,13,16,17,27] have been reported to fabricate active Ni-based catalysts owning the high methanation catalytic activity at low temperatures. Additionally, since the catalytic stability of Ni-based catalyst has remained challenges due to a highly exothermic methanation process, the development of core-shell structural catalysts to prevent carbon deposition and Ni sintering has been reported [28–31]. The core–shell metal@metal oxide particle can be considered as a high thermal-conducting support material given the high thermal conductivity of the metal and good textural properties of the metal oxide layer (e.g., high surface area and enhanced stability against thermal and chemical attack) [32]. Among various core–shell composite candidates, Al@Al_2O_3 can be prepared by the hydrothermal surface oxidation (HTSO) of Al metal particles in an aqueous solution at elevated temperatures (120–200 °C) [33]. It provides superior heat conductivity and

* Corresponding author.
E-mail address: edpark@ajou.ac.kr (E.D. Park).

https://doi.org/10.1016/j.cattod.2019.09.028
Received 19 April 2019; Received in revised form 20 August 2019; Accepted 18 September 2019

surface properties and thus can be regarded as a potential heterogeneous catalyst substrate for highly exothermic and endothermic reactions [33–35].

In this work, the core–shell microstructural Al@Al_2O_3 support was applied as the support for supported Ni catalysts in CO and CO_2 methanation. Two different preparation methods, namely wet impregnation (WI) and deposition–precipitation (DP), were compared for the supported Ni catalysts. Improved catalytic activity was observed over the Ni/Al@Al_2O_3 catalyst prepared by the DP method. The catalytic activity was closely related to Ni dispersion and preferential uptake of the reactant, and these findings were supported by various characterization techniques.

2. Experimental

2.1. Catalyst preparation

The core–shell Al@Al_2O_3 support was prepared by the HTSO method [33]. The detailed procedure is described in the supporting information. The Al@Al_2O_3-supported Ni catalyst prepared from the aqueous solution of $Ni(NO_3)_2{\cdot}6H_2O$ (Junsei Chemical Co., Ltd.) and home-made Al@Al_2O_3 by the conventional WI method is denoted as Ni/Al@Al_2O_3 (WI). For comparison, the Al_2O_3-supported Ni catalyst was also prepared with γ-Al_2O_3 (neutral, Alfa Aesar) by the WI method and is designated as Ni/γ-Al_2O_3 (WI). Both Ni/γ-Al_2O_3 (WI) and Ni/Al@Al_2O_3 (WI) were prepared after calcination in air at 500 ℃ and subsequent reduction in the H_2 stream at 500 ℃. Moreover, the Al@Al_2O_3-supported Ni catalyst was prepared using the DP method. For the DP method, 2.91 g of $Ni(NO_3)_2{\cdot}6H_2O$ (Junsei Chemical Co., Ltd.) was dissolved in 50 mL of deionized (DI) water. This solution was contacted with 5.3 g of Al@Al_2O_3, and 1.0 M aqueous NH_4OH solution (Samchun Pure Chemical Co., Ltd.) was added to this slurry drop by drop until a final pH of 9 was reached under stirring for 12 h at room temperature. The slurry was filtered and washed several times with DI water. The recovered powder was dried in an oven at 110 ℃ for 12 h. This dried sample was further reduced in the H_2 stream at 500 ℃ for 1 h. The resulting catalyst is denoted as Ni/Al@Al_2O_3 (DP110). In order to assess the effect of the calcination temperature, the dried sample was calcined in air at 500 ℃ for 3 h and subsequently reduced in the H_2 stream at 500 ℃ for 1 h to obtain Ni/Al@Al_2O_3 (DP500). The Ni content for all supported Ni catalysts was intended to be 10 wt.% and confirmed using inductively coupled plasma-atomic emission spectroscopy (ICP-AES).

2.2. Catalyst characterization

N_2 physisorption was analyzed using a Micromeritics ASAP 2020 instrument in which the supports and catalysts were degassed under vacuum for 6 h at 200 ℃ before the analysis. The specific surface area (S_{BET}) of the sample was determined according to the Brunauer–Emmett–Teller method. The pore size distribution for each catalyst was obtained using the Barrett–Joyner–Halenda desorption method.

X-ray diffraction (XRD) patterns were detected by a Rigaku D/Max instrument with a Cu Kα source to assess the bulk crystalline structure of the samples.

The temperature-programmed reduction with H_2 (H_2-TPR) was performed with a Micromeritics 2910 Autochem instrument to check the reducibility of the nickel oxide species in the sample. All samples except for Ni/Al@Al_2O_3 (DP110), which was used only in the dried form, were calcined in air at 500 ℃. Then, 0.20 g of the sample was contacted with 10 mol% H_2/Ar at a flow rate of 30 mL/min in the temperature range of 40–900 ℃.

The catalytically active surface area (CASA) and Ni dispersion for each catalyst were determined by H_2 chemisorption using a Micromeritics ASAP 2020 instrument, as described previously [11].

Pulsed CO_2 chemisorption and temperature-programmed desorption (TPD) of CO_2 (CO_2-TPD) were carried out on a Micrometrics Autochem 2910 instrument to analyze the basicity of the catalyst surface. Pulsed CO_2 chemisorption was conducted at room temperature by injection of 0.50 mL of 15 mol% CO_2 balanced with He in a He stream at a flow rate of 30 mL/min. CO_2-TPD was conducted in the He stream at a flow rate of 30 mL/min for the temperature range of 40–900 ˚C at a heating rate of 10 ˚C/min. The ion signals recorded at m/e = 44 were utilized for monitoring the desorbed CO_2.

In-situ diffuse reflectance infrared Fourier transform spectroscopy (DRIFTS) experiments were carried out on a NICOLET 6700 (Thermo Scientific) spectrometer equipped with a ZnSe window with a resolution of 3.857 cm^{-1}. Before CO_2 adsorption, the sample was reduced in-situ in the DRIFTS cell at 500 ˚C for 1 h using H_2 at a flow rate of 30 mL/min, and cooled under He flow to 40 ℃. The cell was purged with He before the introduction of CO_2 at a flow rate of 50 mL/min. A background spectrum was recorded under He flow. CO_2 adsorption was performed for 20 min at 40 ℃, and the spectra were recorded while purging with He at a flow rate of 100 mL/min at different temperatures. The spectra were also recorded during CO and CO_2 methanation under the same reaction conditions as described for the catalytic activity test. At each reaction temperature, the signal was recorded after 20 min of reaction time.

Thermogravimetric analysis (TGA) and differential thermal analysis (DTA) were performed on a thermogravimetric analyzer (NETZSCH STA 409 PC/PG) in air with a flow rate of 50 mL/min from room temperature to 1000 ℃ at a heating rate of 10 ℃/min.

Temperature-programmed oxidation (TPO) was conducted over 0.10 g of each sample in a 2% O_2/He stream by heating the sample in the temperature range of 30–900 ˚C at a heating rate of 10 ℃/min while monitoring the thermal conductivity detector (TCD) signals (Autochem 2910, Micromeritics) and online mass spectrometer signals corresponding to CO_2 (m/z = 44) (Cirrus 2 Quadrupole Mass Spectrometer) after the sample was purged with He at room temperature for 1 h.

High-resolution transmission electron microscopy (HRTEM) images were obtained using Tecnai G2 TEM (FEI) operating at 200 kV with an energy dispersive (EDS) detector.

Inductively coupled plasma-atomic emission spectroscopy (ICP-AES) was carried out on a Thermo Scientific iCAP 6500 instrument to determine the Ni content for each catalyst.

2.3. Catalytic activity test

CO and CO_2 methanation were carried out in a fixed-bed quartz reactor, as described previously [10]. Briefly, 0.10 g of the catalyst with particulate sizes of 45–80 mesh was reduced at 500 ℃ for 1 h in a 30 mL/min H_2 stream and then contacted with the feed gas composed of 1 mol% CO (or CO_2), 50 mol% H_2, and 49 mol% He at a flow rate of 100 mL/min. The reaction was conducted at atmospheric pressure in the reaction temperature range of 140–450 ℃. The kinetic experiments were performed separately at low reaction temperatures under different reaction conditions, wherein 0.10 g of the catalyst was diluted with 0.20 g of α-alumina and then contacted with the feed gas. The CO and CO_2 conversions were controlled to be less than 15%. The activation energy (E_a) over each catalyst was calculated based on the Arrhenius equation.

$$k = A\exp\left(-\frac{E_a}{RT}\right) \tag{3}$$

where k denotes the reaction rate constant, A is the frequency factor, E_a is the activation energy, R is the gas constant, and T is the absolute temperature. The exit gas composition was analyzed using a gas chromatograph (YL Instrument 6100GC), equipped with a packed column filled with Carbosphere® for TCD and a capillary Poralot Q column for the flame ionization detector (FID). CO conversion (X_{CO}), CO_2 conversion (X_{CO_2}), CO yield (Y_{CO}), and C_1-C_3 hydrocarbon yield ($Y_{C_xH_y}$)

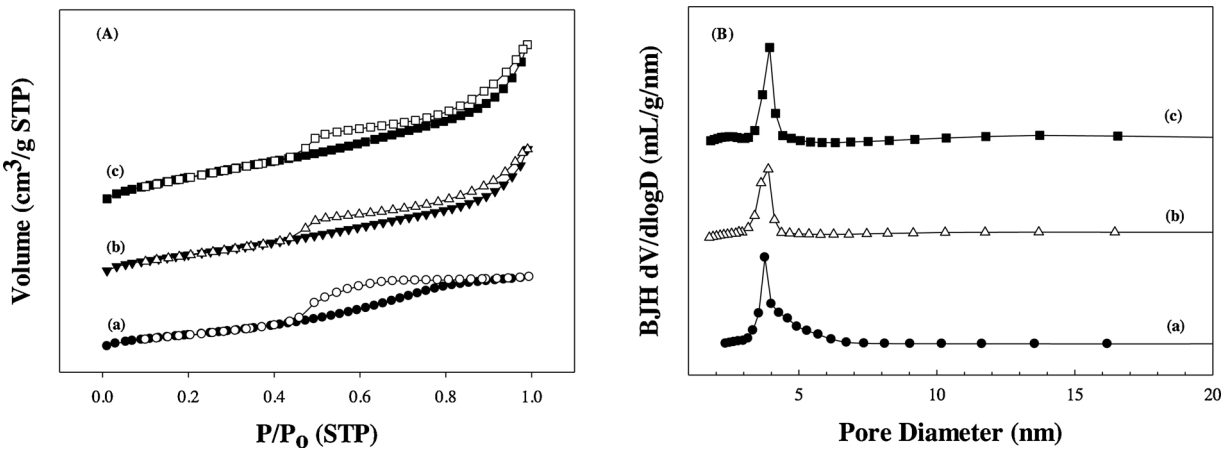

Fig. 1. N_2 adsorption (filled points) and desorption (unfilled points) isotherms (A) and pore size distribution (B) of Ni/Al@Al_2O_3 (WI) (a), Ni/Al@Al_2O_3 (DP110) (b), and Ni/Al@Al_2O_3 (DP500) (c).

were calculated using the following equations.

$$X_{CO}\ (\%) = \frac{[CO]_{in} - [CO]_{out}}{[CO]_{in}} \times 100 \quad (4)$$

$$X_{CO_2}\ (\%) = \frac{[CO_2]_{in} - [CO_2]_{out}}{[CO_2]_{in}} \times 100 \quad (5)$$

$$Y_{C_xH_y}\ (\%) = \frac{x[C_xH_y]_{out}}{[CO]_{in} + [CO_2]_{in}} \times 100 \quad (6)$$

where $[CO]_{in}$, $[CO_2]_{in}$, $[CO]_{out}$, $[CO_2]_{out}$, and $[C_xH_y]_{out}$ are the CO concentration in the feed stream, CO_2 concentration in the feed stream, CO concentration in the exit stream, CO_2 concentration in the exit stream, and C_xH_y concentration in the exit stream, respectively.

3. Results and discussion

3.1. Characterization of the catalysts

Fig. 1A shows the N_2 adsorption and desorption diagram of each catalyst. All catalysts have the type-IIb isotherms [36]. A rather narrow pore diameter distribution was obtained for each Ni/Al@Al_2O_3 catalyst (Fig. 1B). The textural properties of the prepared catalysts probed by N_2 physisorption are summarized in Table 1. Compared with Al@Al_2O_3, whose surface area, pore volume, and average pore diameter were determined to be 142 m^2/g, 0.19 cm^3/g, and 5.4 nm, respectively, Ni/Al@Al_2O_3 (WI) had a smaller surface area, pore volume, and average pore diameter, indicating that the Ni particles were well-dispersed over the support. However, small increases in the specific surface area, pore volume, and average pore diameter were noted for the Ni/Al@Al_2O_3 (DP) catalysts compared with those for the support, indicating that the textural properties of the Al@Al_2O_3 were further modified during the DP process.

In order to study the bulk crystalline structure of the supported Ni catalysts before and after reduction, XRD patterns of all Ni/Al@Al_2O_3 samples were obtained. As shown in Fig. 2, the presence of Al metal was confirmed for all Ni catalysts supported on Al@Al_2O_3 before and after reduction. Note that the XRD peaks due to Al (JCPDS 04-0787) become weaker for Ni/Al@Al_2O_3 prepared by the DP method. This aspect is closely related to the changes in the textural properties of Ni/Al@Al_2O_3 (DP) compared with Ni/Al@Al_2O_3 (WI). Using NH_4OH solution in the DP process caused the partial transformation of the aluminum in the core into α-$Al_2(OOH)_2$ (Fig. 2B) resulting in the decrease in the intensity of the XRD peak due to Al metal. Therefore, the fractions of core Al metal in the Ni/Al@Al_2O_3 (DP) were smaller than that in the Ni/Al@Al_2O_3 (WI), as listed in Table S1. The strong XRD peaks due to NiO (JCPDS 47–1049) were observed for unreduced supported Ni catalysts prepared by the WI method (NiO/Al@Al_2O_3 (WI)). On the other hand, very weak XRD peaks owing to NiO were observed over NiO/Al@Al_2O_3 (DP), indicating the high dispersion of NiO. α-$Al_2(OOH)_2$ and γ-Al_2O_3 were detected for the unreduced NiO/Al@Al_2O_3 (DP110) and NiO/Al@Al_2O_3 (DP500), respectively, as the bulk crystalline phase of aluminum oxides. However, γ-Al_2O_3 was the only phase as aluminum oxide, and all the XRD peaks due to NiO disappeared for all supported Ni catalysts after reduction. The crystallite size of the metallic Ni in the reduced catalyst could not be calculated due to the overlap of XRD peaks corresponding to Ni and Al.

H_2 chemisorption was performed to determine the Ni dispersion and the CASA of all the catalysts. As shown in Table 1, Ni/Al@Al_2O_3 (WI) shows higher Ni dispersion and larger CASA than Ni/γ-Al_2O_3 (WI). Compared with the WI method, a further increase in Ni dispersion and CASA was achieved by adopting the DP method for the Al@Al_2O_3-supported Ni catalyst. In the case of the Ni/Al@Al_2O_3 (DP) catalyst, merely drying and reducing Ni/Al@Al_2O_3 (DP110) facilitates higher Ni dispersion and larger CASA than calcining and reducing Ni/Al@Al_2O_3 (DP500) at 500 °C.

H_2-TPR was carried out to probe the reducibility of NiO in each sample before reduction. Fig. 3 shows that the sample prepared using the WI method show TPR peaks at higher temperatures than the samples prepared using the DP method. It is generally accepted that the TPR peaks at low and high temperatures are due to NiO interacting weakly and strongly with the support, respectively [17,18]. Compared with the TPR profile for Ni/γ-Al_2O_3 (WI), in which only broad TPR peak centered at 680 °C was observed [17], the TPR peak shifted to the lower temperature for Ni/Al@Al_2O_3 (WI). This indicates that the Ni/Al@Al_2O_3 (WI) has weaker interactions between NiO and the support than the Ni/γ-Al_2O_3 (WI). Ni/Al@Al_2O_3 (DP110) was reduced at much lower temperatures than Ni/Al@Al_2O_3 (DP500), which implies that the interaction between NiO and the support was strengthened in the calcination step at 500 °C. The reduction degree of NiO for each supported Ni catalyst was estimated and reported in Table 1. It increased from 45% for Ni/Al@Al_2O_3 (DP500) to 81% for Ni/Al@Al_2O_3 (DP110), confirming the higher reducibility of the Ni/Al@Al_2O_3 (DP110) catalyst. As a result, a larger amount of NiO must be reduced for Ni/Al@Al_2O_3 (DP110) than Ni/Al@Al_2O_3 (DP500) when both samples were reduced at 500 °C. In the case of the samples supported on Al@Al_2O_3, a small negative TPR peak is observed at approximately 600 °C, which can be attributed to the physical melting of the Al core. Based on the H_2-TPR data, Al@Al_2O_3 appears to interact more weakly with NiO than γ-Al_2O_3 and the DP method outperforms the WI method with regard to increasing the reduction degree and fraction of metallic Ni at the same reduction temperature.

In order to assess the surface property of the prepared catalyst, CO_2

Table 1
Physicochemical properties of supported Ni catalysts [a].

Catalyst	Ni content [b] (%)	Specific surface area [c] (m^2/g)	Pore volume [c] (cm^3/g)	Average pore diameter [c] (nm)	Reduction degree[d] (%)	H_2 uptake [d] (mmol/g)	Ni dispersion [e] (%)	CASA[e] (m^2/$g_{cat.}$)	CO_2 uptake [f] (μmol/g)	Ni size [g] (nm)	Ref.
Ni/γ-Al_2O_3 (WI)	9	130	0.22	7.40	8	0.14	1.7	1.2	28	9.0	[17]
Ni/Al@Al_2O_3 (WI)	10	115	0.15	5.30	12	0.24	3.2	2.2	31	5.0	This work
Ni/Al@Al_2O_3 (DP110)	10	172	0.26	6.04	81	1.58	7.5	5.0	42	2.8	This work
Ni/Al@Al_2O_3 (DP500)	10	204	0.32	6.23	45	0.88	5.2	3.5	39	3.7	This work

[a] All catalysts were reduced in H_2 at 500 °C for 1 h.
[b] The Ni content was determined by ICP-AES analysis.
[c] The specific surface area, pore volume, and average pore diameter were determined by N_2 physisorption.
[d] The reduction degree of NiO and H_2 uptake in the temperature range of 40–500 °C were calculated based on H_2-TPR.
[e] Determination of Ni dispersion and catalytically active surface area (CASA) was based on H_2 chemisorption.
[f] The amount of chemisorbed CO_2 was measured at room temperature.
[g] Estimation of the particle size of Ni was based on the HRTEM images.

chemisorption and CO_2-TPD were carried out to measure the number of basic surface sites and the strengths of the basic sites, respectively. As listed in Table 1, the amounts of chemisorbed CO_2 for Ni/γ-Al_2O_3 (WI), Ni/Al@Al_2O_3 (WI), Ni/Al@Al_2O_3 (DP110), and Ni/Al@Al_2O_3 (DP500) are 28, 31, 42, and 39 μmol/g, respectively. This result implies that the DP method provides a larger number of basic sites than the WI method. Fig. 4 reveals that similar CO_2-TPD patterns were obtained for Ni/γ-Al_2O_3 (WI) and Ni/Al@Al_2O_3 (WI), wherein a desorption peak at approximately 100 °C, assigned to CO_2 desorption from weak basic sites, was observed [11,15]. The only difference between these patterns is the latter shows a TPD peak maximum at a higher temperature than the former, indicating that the basic sites of Ni/Al@Al_2O_3 (WI) can interact with CO_2 more strongly than Ni/γ-Al_2O_3 (WI). Interestingly, the Ni/Al@Al_2O_3 (DP) samples show additional CO_2-TPD peaks in the temperature range of 200–350 °C compared with the samples prepared by the WI method. This result implies that the DP method provides the additional moderate basic sites, which cannot be formed by the WI method. These moderate basic sites have been reported to be favorable for the activation of CO_2 [12,13,25,37]. The comparison between Ni/Al@Al_2O_3 (DP110) and Ni/Al@Al_2O_3 (DP500) reveals that there is the slight shift of moderate basic sites to a higher temperature for the former catalyst, demonstrating the stronger binding of CO_2 on the former catalyst compared with the latter one. Additionally, very weak CO_2-TPD peaks were also observed in the temperature range of 550 to 750 °C. However, these strong basic sites might have a limited effect on the catalytic activity for CO_2 methanation because of their weak peak intensity. Each band corresponding to a different basic site over each catalyst was deconvoluted and quantified in Table S2. The fraction of strong basic site (peak δ) for all samples was below 0.05. The total area for each catalyst from the CO_2-TPD profile in Table S2 is consistent with the CO_2 uptake measured at room temperature in Table 1.

Fig. 5 illustrates the TEM images of the Al@Al_2O_3-supported Ni catalysts. As revealed in the particle size distribution of Ni metal (Fig. S1), a rather uniform particle size distribution of Ni metal can be found for Ni/Al@Al_2O_3 (DP) catalysts compared with Ni/Al@Al_2O_3 (WI). The average particle sizes of Ni metal for Ni/Al@Al_2O_3 (DP110) and Ni/Al@Al_2O_3 (DP500) are determined to be 2.8 and 3.7 nm, respectively. Conversely, the slight agglomeration of Ni particles is observed for Ni/Al@Al_2O_3 (WI) catalyst, with the mean particle size of Ni being approximately 5.0 nm. The measurements are consistent with the H_2 chemisorption data, which shows that Ni dispersion decreases with increasing average Ni particle size. The average particle size of Ni increases in the following order: Ni/Al@Al_2O_3 (DP110) < Ni/Al@Al_2O_3 (DP500) < Ni/Al@Al_2O_3 (WI). Moreover, the typical STEM dark field image and corresponding elemental maps confirm that the Ni, Si, and O elements are well distributed in each sample (Fig. 5).

3.2. CO methanation

The catalytic activity for CO methanation over the supported Ni catalysts was evaluated, and the CO conversions as a function of the reaction temperature are displayed in Fig. S2A. The catalytic activity increased in the following order: Ni/γ-Al_2O_3 (WI) < Ni/Al@Al_2O_3 (WI) < Ni/Al@Al_2O_3 (DP500) < Ni/Al@Al_2O_3 (DP110). Note that Al@Al_2O_3 outperformed γ-Al_2O_3 and that the DP method is better than the WI method for achieving high catalytic activity for CO methanation. This catalytic activity is directly related to Ni dispersion and CASA. In terms of product selectivity, CH_4 is a predominant product at all reaction temperatures, while C_2H_6 and C_3H_8 are also detected as byproducts (Fig. S3). The Arrhenius plots for the CH_4 formation rate under CO methanation over all the catalysts were determined and are presented in Fig. 6A. The Ni/Al@Al_2O_3 (DP110) catalyst shows the highest CH_4 formation rate and has the lowest apparent activation energy (95 kJ/mol) among the tested catalysts. The activation energies were determined to be 110, 103, and 96 kJ/mol for Ni/γ-Al_2O_3 (WI), Ni/Al@Al_2O_3 (WI), and Ni/Al@Al_2O_3 (DP500), respectively. The activity

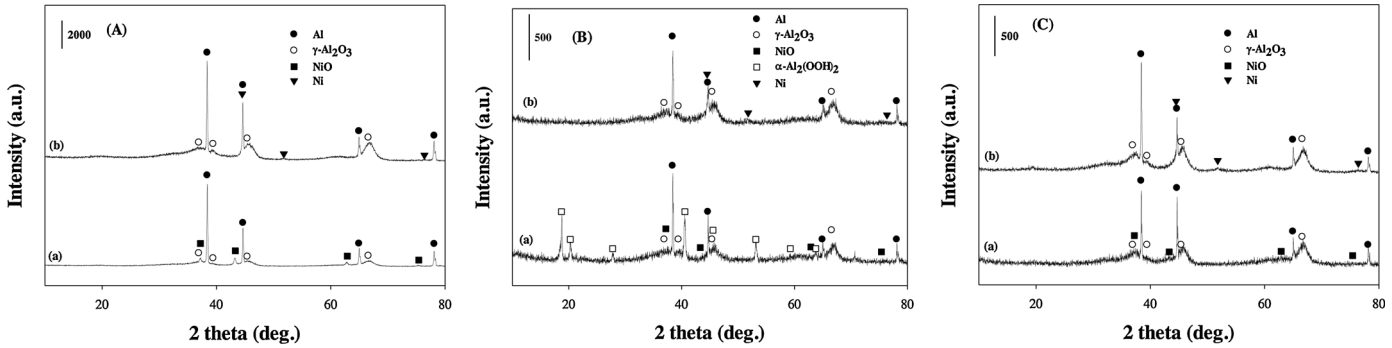

Fig. 2. X-ray diffraction patterns of Ni/Al@Al_2O_3 (WI) (A), Ni/Al@Al_2O_3 (DP110) (B), and Ni/Al@Al_2O_3 (DP500) (C) before (a) and after reduction at 500 °C (b). (●) Al (JCPDS 04-0787), (○) γ–Al_2O_3 (JCPDS 29-0063), (■) NiO (JCPDS 47–1049), (▼) Ni (JCPDS 04-0850), and (□) α-$Al_2(OOH)_2$ (JCPDS 05-0190).

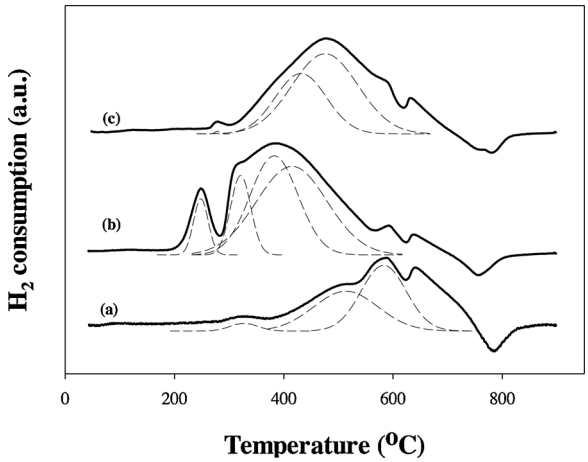

Fig. 3. H_2-TPR profiles of Ni/Al@Al_2O_3 (WI) (a), Ni/Al@Al_2O_3 (DP110) (b), and Ni/Al@Al_2O_3 (DP500) (c). The deconvoluted peaks are plotted in a dashed line.

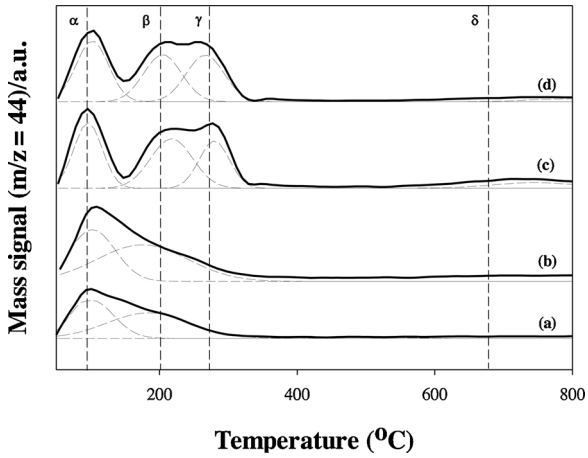

Fig. 4. CO_2-TPD profiles of Ni/γ-Al_2O_3 (WI) (a), Ni/Al@Al_2O_3 (WI) (b), Ni/Al@Al_2O_3 (DP110) (c), and Ni/Al@Al_2O_3 (DP500) (d). The deconvoluted peaks are plotted in a dashed line.

comparison for CO methanation between the Ni/Al@Al_2O_3 catalysts and other supported Ni catalysts reported previously reveals that the Ni/Al@Al_2O_3 catalysts are superior to their counterparts in terms of the CH_4 formation rate under similar reaction conditions (Table S3). All the catalysts are reported to have activation energies ranging from 69 to 132 kJ/mol (Table S3).

3.3. CO_2 methanation

The catalytic activity for CO_2 methanation was measured over the supported Ni catalysts, and the CO_2 conversions at different reaction temperatures are presented in Fig. S2B. Similar to the results for CO methanation, Ni/Al@Al_2O_3 (DP110) shows the highest catalytic activity for CO_2 methanation among the tested catalysts. This catalytic activity is related to the CASA, CO_2 uptake capacity, and binding strength of CO_2 onto the catalyst. The CASA is critical to supply a high concentration of surface H for the hydrogenation of intermediate species in the rate-determining step [16,17]. The high CO_2 uptake capacity and strong interactions between CO_2 and the catalyst surface are also essential for the high catalytic activity needed for CO_2 methanation [9,12,15,37]. The Arrhenius plots for the CH_4 formation rate under CO_2 methanation over the supported Ni catalysts are displayed in Fig. 6B. Ni/Al@Al_2O_3 (DP110) has the highest CH_4 formation rate and the lowest apparent activation energy (74 kJ/mol) among the tested catalysts. The apparent activation energies of Ni/γ-Al_2O_3 (WI), Ni/Al@Al_2O_3 (WI), and Ni/Al@Al_2O_3 (DP500) were determined to be 99, 79, and 77 kJ/mol, respectively. The results are comparable to previous reports (Table S4) in which the activation energies for CO_2 methanation were found to be 80 kJ/mol and 89 kJ/mol over 10 wt.% Ni/Al_2O_3 [38] and 10 wt.% Ni/SiO_2 [18], respectively. During CO_2 methanation, only CH_4 was formed over all the catalysts (Fig. S4). The activity comparison for CO_2 methanation between the Ni/Al@Al_2O_3 catalysts and other supported Ni catalysts reported previously reveals that the Ni/Al@Al_2O_3 catalysts are superior to their counterparts in terms of the CH_4 formation rate under similar reaction conditions (Table S4).

3.4. CO and CO_2 methanation mechanism

In order to probe the surface species during CO methanation over the best Ni/Al@Al_2O_3 (DP110), in-situ DRIFTS spectra were obtained by increasing temperature from 100 to 300 °C as shown in Fig. 7. The recorded spectra at 2180 cm^{-1} is ascribed to $Al^{3+}-CO$ originated from CO adsorption on Al_2O_3 at low temperatures [39]. Its intensity decreased with increasing temperature above 200 °C. Besides, the band which appears at 2120 cm^{-1} suggests the linear C═O vibration of Ni−CO species, which rapidly vanished to form the subcarbonyl Ni species at 2060 cm^{-1} [40] while increasing the reaction temperature. These subcarbonyl Ni species are present alongside the linear carbonyls (2023–2043 cm^{-1}) [41], which were consumed to form CH_4 at 1304 and 3016 cm^{-1} as the reaction temperature increased. The linear CO species are more active than the bridged CO species (1845 - 1930 cm^{-1}) toward CO hydrogenation. The C−H bending mode at 1392 cm^{-1} was detected from 150 °C, whereas the C−H stretching modes are somewhat covered by the rotational fine structure of CH_4 [40]. Moreover, the adsorbed species at 1590 and 2904 cm^{-1} matched formate species, which were formed due to H-assisted C−O bond breaking and the partial dehydroxylation on Al_2O_3 surface at low temperatures [40]. The

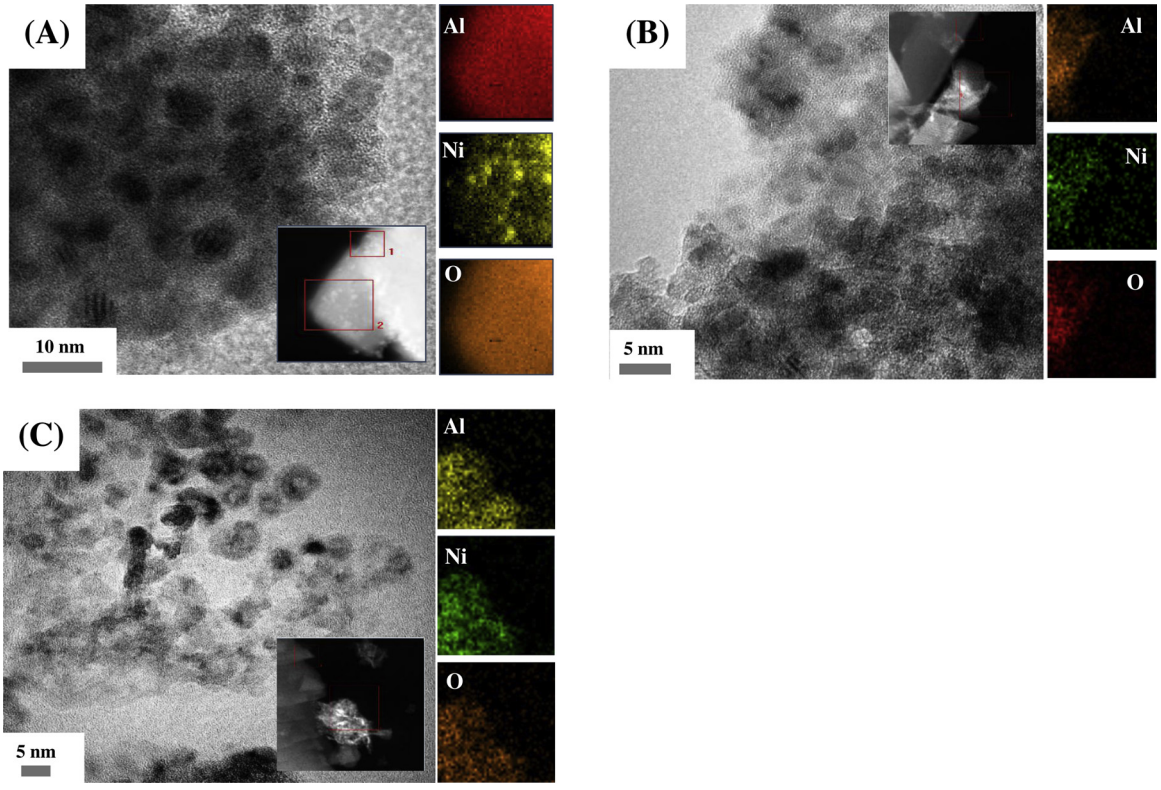

Fig. 5. HRTEM images, and elemental mapping of (A) Ni/Al@Al_2O_3 (WI), (B) Ni/Al@Al_2O_3 (DP110), and (C) Ni/Al@Al_2O_3 (DP500).

formate species were then further hydrogenated to CH_4.

In-situ DRIFTS experiments were performed to study the evolution of surface species during CO_2 methanation over the Ni/γ-Al_2O_3 (WI), Ni/Al@Al_2O_3 (WI), Ni/Al@Al_2O_3 (DP500), and Ni/Al@Al_2O_3 (DP110) catalysts. Fig. 8 shows the infrared spectra recorded after the adsorption of CO_2 for 20 min at 40 °C and 300 °C to differentiate basic surface sites. Three different basic sites on the catalyst can be distinguished: bicarbonate (at ν = 1650, 1450, and 1230 cm^{-1}), monodentate carbonate (ν = 1390 and 1530 cm^{-1}), and bidentate carbonate (ν = 1590 and 1320 cm^{-1}) [12,37,42–45]. Each band corresponding to a different basic site was deconvoluted (Fig. S5) and quantified as seen in Table 2. The fraction of moderate basic sites forming bidentate carbonate and strong basic sites responsible for monodentate carbonate [12,22,37,42] seems to be slightly higher for the Ni/Al@Al_2O_3 (DP) catalysts. On the other hand, the fraction of weak basic sites forming bicarbonate seems to be high for Ni/γ-Al_2O_3 (WI) and Ni/Al@Al_2O_3 (WI). Ni/Al@Al_2O_3 (DP110) appears to have the highest ratio of total medium and strong basic sites to weak basic sites, which is consistent with the CO_2-TPD profiles described in Fig. 4 and percentage of peak-fitting data observed in Table S2. The Ni catalysts supported on Al@Al_2O_3 are confirmed to possess higher densities of medium and strong basic sites than Ni/γ-Al_2O_3 (WI), which is beneficial for the high catalytic activity required for CO_2 methanation [9,12,15,25,37].

Fig. 9 shows the various surface intermediates formed during CO_2 methanation in the temperature range of 150–400 °C. New bands appear at 3016, 2904, 1595, 1376, and 1304 cm^{-1} while the bands corresponding to carbonates at 1650, 1530, 1440, and 1230 cm^{-1} are attenuated at low reaction temperatures. The peaks at 3016 and 1304 cm^{-1} are assigned to CH_4 [9,25,46,47]. The peaks at 2904, 1595, and 1376 cm^{-1} correspond to bidentate formate species and the band at 1340 cm^{-1} is assigned to monodentate formate species [9,12,13,18,23,25,46]. With increasing reaction temperature, the bands of formate species reached a maximum at 300 °C with the continuous consumption of carbonates, suggesting the transformation of

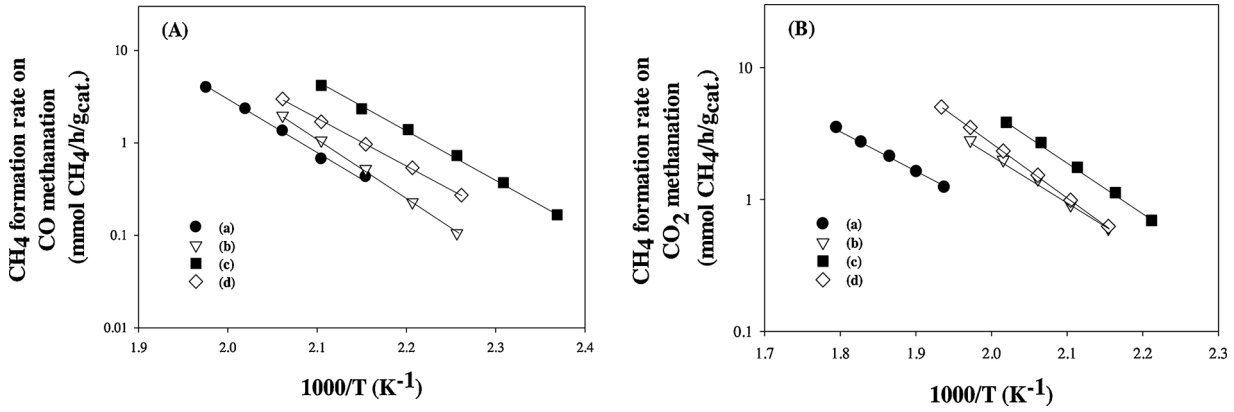

Fig. 6. CH_4 formation rate of Ni/γ-Al_2O_3 (WI) (a), Ni/Al@Al_2O_3 (WI) (b), Ni/Al@Al_2O_3 (DP110) (c), and Ni/Al@Al_2O_3 (DP500) (d) on: (A) CO methanation and (B) CO_2 methanation. All the catalysts were reduced in H_2 at 500 °C. Reaction conditions: 1 mol% CO/CO_2, 50 mol% H_2, 49 mol% He, F/W = 1000 mL/min/$g_{cat.}$

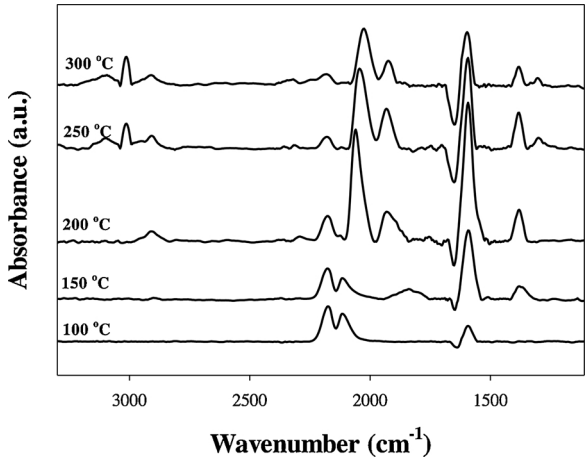

Fig. 7. In situ DRIFTS during CO methanation over Ni/Al@Al_2O_3 (DP110) from 100 to 300 °C. The catalyst was contacted with the feed gas composed of 1 mol % CO, 50 mol% H_2, and 49 mol% He with a total flow of 50 mL/min.

carbonates into formate species in the presence of H_2. The monodentate formate species are reported to react more quickly with H_2 than the bidentate formate species [13,18]. The peaks of the formate species decrease with the continuous formation of surface CH_4 species. Therefore, it can be said that the possible complete reaction route of the CO_2 methanation over the Ni/Al@Al_2O_3 (DP110) catalyst is as follows. CO_2 is first chemisorbed onto the catalyst surface to form carbonates. Then, it is hydrogenated into formate, and finally, it transforms into CH_4. This is consistent with the findings of past studies [9,13,18,37]. There are two main different opinions on the CH_4 formation process and the nature of the intermediate involved in CO_2 methanation. The first is that the process might involve the conversion of CO_2 to CO before being hydrogenated to CH_4 [47–49]. The second posits the direct hydrogenation of CO_2 to CH_4 without forming a CO intermediate [9,18,37,46,49]. In this study, no CO was observed under the given reaction conditions, which suggests that the catalytic mechanism might not involve the CO intermediate.

3.5. Stability evaluation

The most active catalyst, Ni/Al@Al_2O_3 (DP110), was selected in order to evaluate the catalyst stability during CO and CO_2 methanation. As shown in Fig. 10, CO and CO_2 conversions decreased slowly in the first 10 h of operation but showed steady-state values for the remaining time. The change in the CO or CO_2 conversions during the stability test was less than 3%. The results of the XRD analysis confirm that the bulk crystalline structure is maintained (Fig. S6). No XRD peak is detected for crystalline carbon (graphite or whisker carbon) and NiO. There is no noticeable change in the relative peak intensity attributable to Al and γ-Al_2O_3 for the catalyst after the stability test, indicating that the core–shell structure is maintained. No apparent morphological change is observed via TEM analysis after the stability test (Fig. S7). However, the particle size of Ni appears to have increased slightly from 2.8 to 3.8 nm after the stability test.

Table 2
Basic site distribution of each Ni-based catalyst determined by deconvolution of DRIFTS spectra after CO_2 adsorption at 300 °C.

Catalyst	Percent of each basic site in wavenumber range 1130–1910 cm^{-1} (%)		
	Weak basic sites	Moderate basic sites	Strong basic sites
Ni/γ-Al_2O_3 (WI)	55.5	11.6	32.9
Ni/Al@Al_2O_3 (WI)	46.3	11.8	41.9
Ni/Al@Al_2O_3 (DP110)	27.4	36.6	36.0
Ni/Al@Al_2O_3 (DP500)	42.2	12.0	45.8

TGA and DTA analyses of the fresh and spent catalysts were also performed to monitor the weight loss in the sample as a function of temperature. The TGA curves show a weight-loss up to 8% from room temperature to 600 °C (Fig. S8). The small difference (of up to 1%) in the TGA profiles between the fresh and spent samples, and the overlapping of the DTG curves indicate negligible coke deposition. Moreover, TPO profiles confirm slight coke deposition in the spent catalysts (Fig. S9). The amount of CO_2 produced during the TPO experiments appears to be larger after CO methanation than that after CO_2 methanation. In conclusion, the Ni/Al@Al_2O_3 (DP) catalyst calcined at low temperatures and subsequently reduced, exhibiting high Ni dispersion, large CASA, and stable catalytic activity.

4. Conclusions

The outstanding catalytic performance of the Ni catalysts supported on core–shell Al@Al_2O_3 with regard to both CO and CO_2 methanation owing to the high dispersion of Ni and high reduction degree of NiO nanoparticles offers insights into a new catalyst design strategy. Deposition–precipitation with mild thermal pretreatment is confirmed

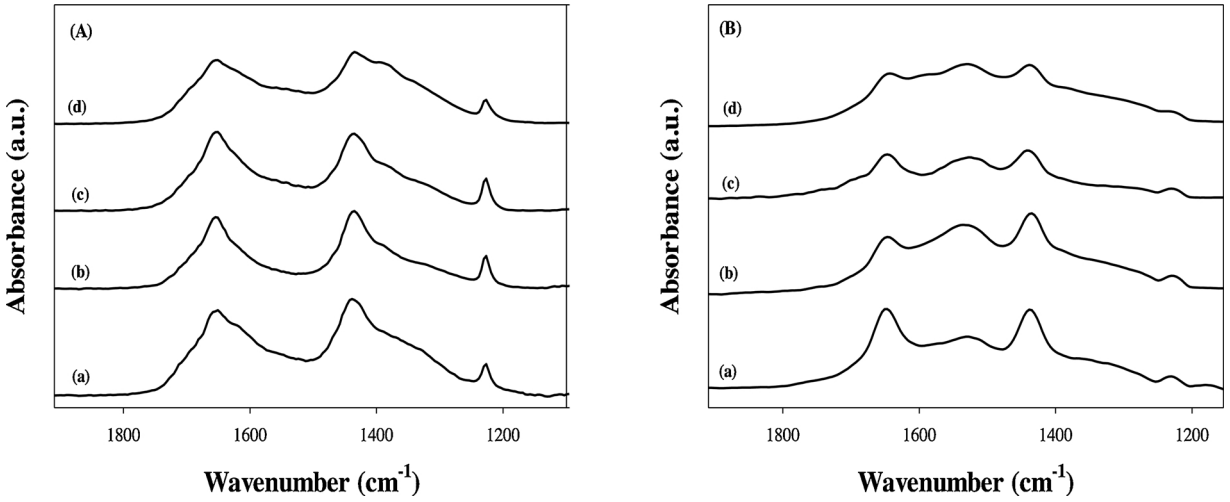

Fig. 8. In situ DRIFTS after CO_2 adsorption at 40 °C (A) and 300 °C (B) on (a) Ni/γ-Al_2O_3 (WI), (b) Ni/Al@Al_2O_3 (WI), (c) Ni/Al@Al_2O_3 (DP110), and (d) Ni/Al@Al_2O_3 (DP500).

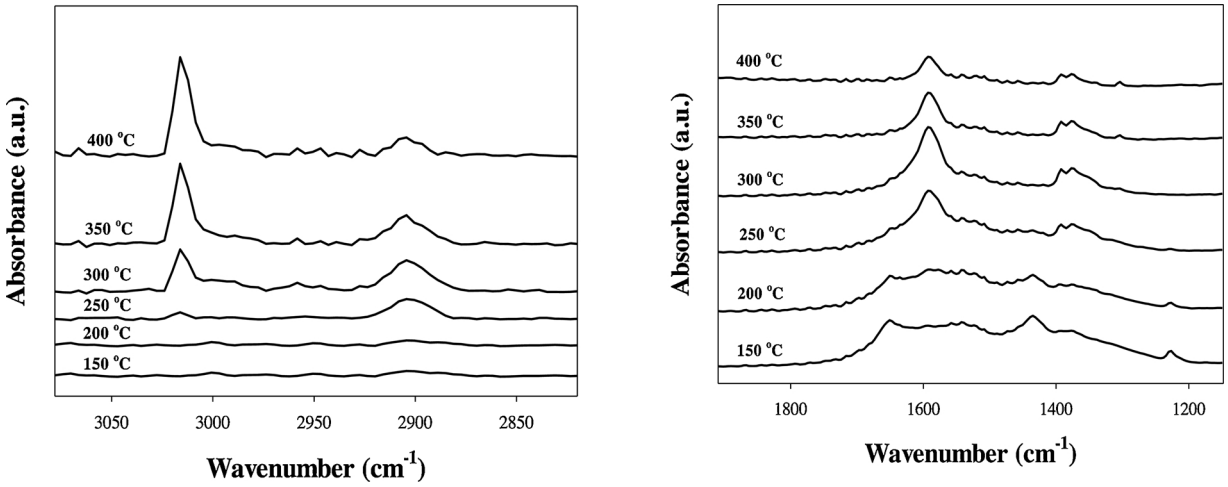

Fig. 9. In situ DRIFTS during CO_2 methanation over Ni/Al@Al_2O_3 (DP110) from 150 to 400 °C. The catalyst was contacted with the feed gas composed of 1 mol% CO_2, 50 mol% H_2, and 49 mol% He with a total flow of 50 mL/min.

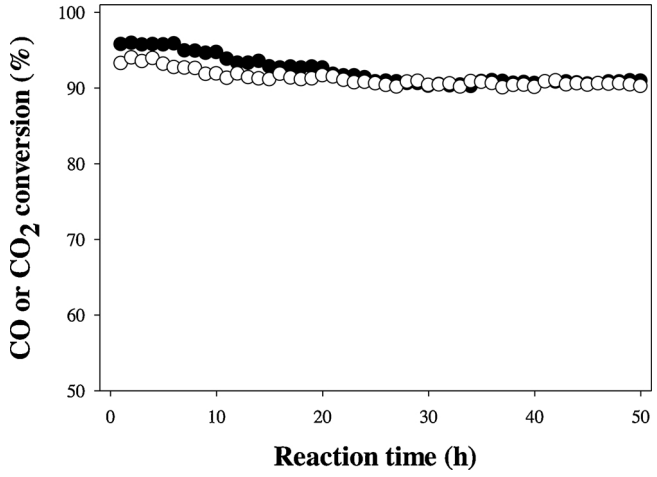

Fig. 10. Stability test for Ni/Al@Al_2O_3 (DP110) for CO methanation at 240 °C (●) and CO_2 methanation at 310 °C (○) for 50 h. Reaction conditions for CO and CO_2 methanation were the same as those in Fig. 6.

as a more effective preparation method to enhance catalytic activity compared with the conventional WI method. The CO_2 methanation over the Ni/Al@Al_2O_3 (DP) catalyst is considered to occur with the carbonate and formate species as the intermediates. The binding strength of CO_2 and the number of basic sites play a key role in the CO_2 methanation. The catalytic activity for both CO and CO_2 methanation is confirmed to be stable over Ni/Al@Al_2O_3 (DP110), with high coking resistance for 50 h.

Acknowledgments

This work was supported by the Human Resources Program in Energy Technology (No. 20154010200820) of the Korea Institute of Energy Technology Evaluation and Planning (KETEP), which receives financial grants from the Ministry of Trade, Industry and Energy of the Republic of Korea. This work was also supported by the C1 Gas Refinery Program through the National Research Foundation of Korea (NRF) funded by the Ministry of Science, ICT & Future Planning (2015M3D3A1A01064899)

Appendix A. Supplementary data

Supplementary material related to this article can be found, in the online version, at doi:https://doi.org/10.1016/j.cattod.2019.09.028.

References

[1] B. Hu, C. Guild, S.L. Suib, J. CO_2 Util. 1 (2013) 18–27.
[2] M. Cokoja, M.E. Wilhelm, M.H. Anthofer, W.A. Herrmann, F.E. Kühn, ChemSusChem 8 (2015) 2436–2454.
[3] M.D. Porosoff, B. Yan, J.G. Chen, Energ. Environ. Sci. 9 (2016) 62–73.
[4] G. Centi, E.A. Quadrelli, S. Perathoner, Energ. Environ. Sci. 6 (2013) 1711–1731.
[5] A. ElMekawy, H.M. Hegab, G. Mohanakrishna, A.F. Elbaz, M. Bulut, D. Pant, Bioresour. Technol. 215 (2016) 357–370.
[6] J. Klankermayer, S. Wesselbaum, K. Beydoun, W. Leitner, Angew. Chem. Int. Ed. 55 (2016) 7296–7343.
[7] M. Götz, J. Lefebvre, F. Mörs, A. McDaniel Koch, F. Graf, S. Bajohr, R. Reimert, T. Kolb, Renew. Energ. 85 (2016) 1371–1390.
[8] A. Molino, S. Chianese, D. Musmarra, J. Energ. Chem. 25 (2016) 10–25.
[9] J. Ashok, M.L. Ang, S. Kawi, Catal. Today 281 (2017) 304–311.
[10] T.A. Le, M.S. Kim, S.H. Lee, T.W. Kim, E.D. Park, Catal. Today 293-294 (2017) 89–96.
[11] T.A. Le, T.W. Kim, S.H. Lee, E.D. Park, Korean J. Chem. Eng. 34 (2017) 3085–3091.
[12] T. Burger, F. Koschany, O. Thomys, K. Köhler, O. Hinrichsen, Appl. Catal. A Gen. 558 (2018) 44–54.
[13] X. Guo, Z. Peng, M. Hu, C. Zuo, A. Traitangwong, V. Meeyoo, C. Li, S. Zhang, Ind. Eng. Chem. Res. 57 (2018) 9102–9111.
[14] T.A. Le, J.K. Kang, E.D. Park, Top. Catal. 61 (2018) 1537–1544.
[15] A. Vita, C. Italiano, L. Pino, P. Frontera, M. Ferraro, V. Antonucci, Appl. Catal. B 226 (2018) 384–395.
[16] D. Beierlein, D. Häussermann, M. Pfeifer, T. Schwarz, K. Stöwe, Y. Traa, E. Klemm, Appl. Catal. B 247 (2019) 200–219.
[17] T.A. Le, J.K. Kang, S.H. Lee, E.D. Park, J. Nanosci. Nanotechnol. 19 (2019) 3252–3262.
[18] X. Guo, A. Traitangwong, M. Hu, C. Zuo, V. Meeyoo, Z. Peng, C. Li, Energ. Fuel. 32 (2018) 3681–3689.
[19] M. Li, H. Amari, A.C. van Veen, Appl. Catal. B 239 (2018) 27–35.
[20] Y. Yu, Z. Bian, F. Song, J. Wang, Q. Zhong, S. Kawi, Top. Catal. 61 (2018) 1514–1527.
[21] Y. Yu, Y.M. Chan, Z. Bian, F. Song, J. Wang, Q. Zhong, S. Kawi, Int. J. Hydrog. Energ. 43 (2018) 15191–15204.
[22] E.M. Köck, M. Kogler, T. Bielz, B. Klötzer, S. Penner, J. Phys. Chem. C 117 (2013) 17666–17673.
[23] M.C. Bacariza, I. Graça, S.S. Bebiano, J.M. Lopes, C. Henriques, Chem. Eng. Sci. 175 (2018) 72–83.
[24] T.A. Le, J.K. Kang, E.D. Park, Appl. Catal. A Gen. 581 (2019) 67–73.
[25] Y. Yan, Y. Dai, Y. Yang, A.A. Lapkin, Appl. Catal. B 237 (2018) 504–512.
[26] E. Jwa, S.B. Lee, H.W. Lee, Y.S. Mok, Fuel Process. Technol. 108 (2013) 89–93.
[27] K. Stangeland, D. Kalai, H. Li, Z. Yu, Energ. Procedia 105 (2017) 2022–2027.
[28] Z. Li, Z. Wang, S. Kawi, ChemCatChem 11 (2019) 202–224.
[29] Z. Li, M. Li, Z. Bian, Y. Kathiraser, S. Kawi, Appl. Catal. B 188 (2016) 324–341.
[30] P. Lakshmanan, M.S. Kim, E.D. Park, Appl. Catal. A Gen. 513 (2016) 98–105.
[31] Y. Han, B. Wen, M. Zhu, Catalysts 7 (2017).
[32] Q. Zhang, I. Lee, J.B. Joo, F. Zaera, Y. Yin, Acc. Chem. Res. 46 (2013) 1816–1824.
[33] J. Kim, D. Lee, Top. Catal. 58 (2015) 375–385.
[34] T.A. Le, J. Kim, Y.R. Jeong, E.D. Park, Catalysts 9 (2019) 599–610.
[35] T.A. Le, J. Kim, J.K. Kang, E.D. Park, Catal. Today (2019), https://doi.org/10.1016/j.cattod.2019.08.058.
[36] F. Rouquerol, J. Rouquerol, K.S.W. Sing, G. Maurin, P. Llewellyn, 1 - introduction, in: F. Rouquerol, J. Rouquerol, K.S.W. Sing, P. Llewellyn, G. Maurin (Eds.),

Adsorption by Powders and Porous Solids, second edition, Academic Press, Oxford, 2014, pp. 1–24.
[37] Q. Pan, J. Peng, T. Sun, S. Wang, S. Wang, Catal. Commun. 45 (2014) 74–78.
[38] G. Garbarino, D. Bellotti, P. Riani, L. Magistri, G. Busca, Int. J. Hydrog. Energ. 40 (2015) 9171–9182.
[39] A.S. Ivanova, E.M. Slavinskaya, R.V. Gulyaev, V.I. Zaikovskii, O.A. Stonkus, I.G. Danilova, L.M. Plyasova, I.A. Polukhina, A.I. Boronin, Appl. Catal. B 97 (2010) 57–71.
[40] J. Zarfl, D. Ferri, T.J. Schildhauer, J. Wambach, A. Wokaun, Appl. Catal. A Gen. 495 (2015) 104–114.
[41] M.L. Ang, J.T. Miller, Y. Cui, L. Mo, S. Kawi, Catal. Sci. Technol. 6 (2016) 3394–3409.
[42] J.I. Di Cosimo, V.K. Díez, M. Xu, E. Iglesia, C.R. Apesteguía, J. Catal. 178 (1998) 499–510.
[43] S.E. Collins, M.A. Baltanás, A.L. Bonivardi, J. Phys. Chem. B 110 (2006) 5498–5507.
[44] K. Coenen, F. Gallucci, B. Mezari, E. Hensen, M. van Sint Annaland, J. CO_2 Util. 24 (2018) 228–239.
[45] J. Szanyi, J.H. Kwak, Phys. Chem. Chem. Phys. 16 (2014) 15117–15125.
[46] A. Solis-Garcia, J.F. Louvier-Hernandez, A. Almendarez-Camarillo, J.C. Fierro-Gonzalez, Appl. Catal. B 218 (2017) 611–620.
[47] S. Eckle, H.-G. Anfang, R.J. Behm, J. Phys. Chem. C 115 (2011) 1361–1367.
[48] X. Wang, H. Shi, J.H. Kwak, J. Szanyi, ACS Catal. 5 (2015) 6337–6349.
[49] B. Miao, S.S.K. Ma, X. Wang, H. Su, S.H. Chan, Catal. Sci. Technol. 6 (2016) 4048–4058.